Matter

Article

Controllable interlocking from irregularity in two-phase composites

Graphical abstract

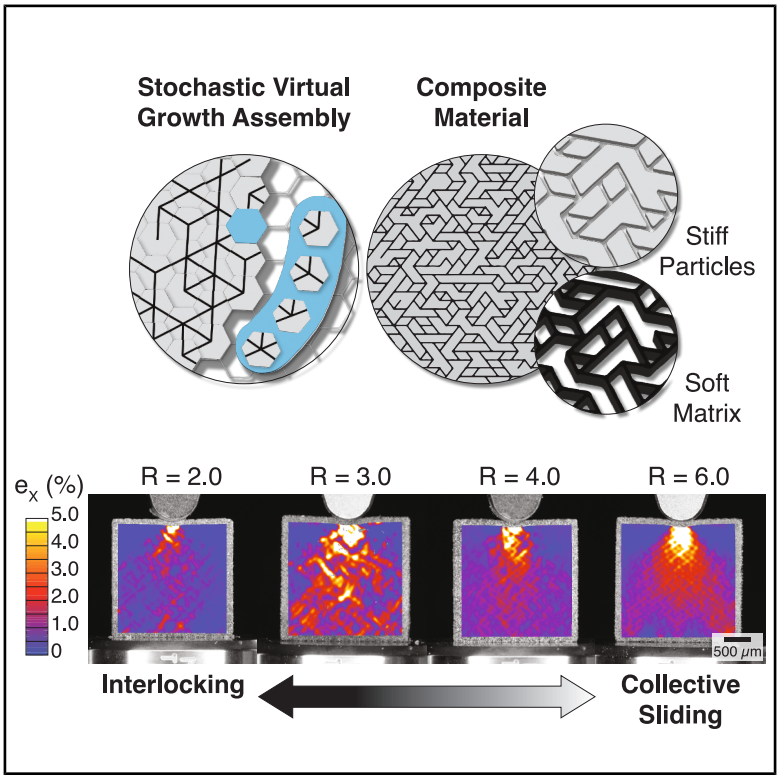

Authors

Chelsea Fox, Kyrillos Bastawros, Tommaso Magrini, Chiara Daraio

Correspondence

t.magrini@tue.nl (T.M.), daraio@caltech.edu (C.D.)

In brief

Inspired by the structure of strong and tough biological materials, we present a new class of two-phase composites with controllable interlocking. The composites feature tessellations of stiff particles connected with a soft matrix and are generated using a stochastic virtual growth algorithm. Irregularity in particle size, geometry, and arrangement controls the degree of interlocking, providing new design principles for tailorable bioinspired deformation mechanisms.

Highlights

- New class of bioinspired two-phase composites with controllable interlocking
- Composites feature tessellations of stiff particles connected with a soft matrix
- Composites are generated using a stochastic virtual growth algorithm
- Irregularity in particle size, geometry, and arrangement controls interlocking

1 Discovery
A new material or phenomena

Fox et al., 2025, Matter *8*, 102201
October 1, 2025
https://doi.org/10.1016/j.matt.2025.102201

CellPress

Please cite this article in press as: Fox et al., Controllable interlocking from irregularity in two-phase composites, Matter (2025), https://doi.org/10.1016/j.matt.2025.102201

Matter

CellPress

Article

Controllable interlocking from irregularity in two-phase composites

Chelsea Fox,[1] Kyrillos Bastawros,[1] Tommaso Magrini,[2,*] and Chiara Daraio[1,3,*]
[1]Division of Engineering and Applied Science, California Institute of Technology, Pasadena, CA 91125, USA
[2]Department of Mechanical Engineering, Eindhoven University of Technology, Eindhoven 5600MB, the Netherlands
[3]Lead contact
*Correspondence: t.magrini@tue.nl (T.M.), daraio@caltech.edu (C.D.)
https://doi.org/10.1016/j.matt.2025.102201

PROGRESS AND POTENTIAL Natural materials often feature a combination of soft and stiff phases, which are arranged to achieve excellent mechanical properties such as high stiffness, strength, and toughness. Many natural materials have even independently evolved similar structures to obtain these properties. Interlocking structures, for example, are common in strong and tough materials and can be observed across many length scales. Inspired by these materials, we present a class of two-phase composites with controllable interlocking. The composites feature tessellations of stiff particles connected by a soft matrix, and we control the degree of interlocking through irregularity in particle size, geometry, and arrangement. We generate the composites through stochastic network growth, which is parameterized by network coordination number alone, demonstrating how irregularity facilitates deformation mechanism control. The study provides new design principles for composites with tailorable bioinspired deformation mechanisms.

SUMMARY

Inspired by strong and tough biological materials, we present composite materials with controllable interlocking. The composites feature tessellations of stiff particles connected by a soft matrix, and we control the degree of interlocking through irregularity in particle size, geometry, and arrangement. We generate the composites through stochastic network growth using an average network coordination number. The generated network forms the soft matrix phase of the composites, while the areas enclosed by the network form the stiff reinforcing particles. At low coordination, composites feature highly polydisperse particles with irregular geometries arranged non-periodically. In response to loading, these particles interlock and primarily rotate and deform to accommodate non-uniform kinematic constraints from adjacent particles. In contrast, higher-coordination composites feature more monodisperse particles with uniform geometries, which collectively slide. We quantify how to control the degree of interlocking as a function of coordination number alone, demonstrating how irregularity facilitates bioinspired deformation mechanism control.

INTRODUCTION

Nature offers an abundance of materials with excellent mechanical properties, including high stiffness,[1–6] high strength,[2–4,7–11] high toughness,[1,4,5,10,12–15] and good energy absorption.[16–18] These materials are often composed of stiff and soft phases arranged to optimize mechanical performance. Many biological materials have even independently evolved to have similar structures across a wide range of length scales.[19] For example, interlocking structures that provide excellent mechanical performances can be observed in many different biological materials, providing high strength, ductility, and toughness.[19] In nacre, interlocking occurs as a result of rough, wavy tablets, which jam as they slide past one another,[1,20,21] while in turtle carapaces and cranial bone, interlocking is seen in zigzag bone interfaces, which engage like puzzle pieces for improved bending strength and toughness.[11,14,22] Interlocking is even seen in stomatopod dactyl clubs, which feature Bouligand and herringbone structures that deflect cracks with out-of-plane interlocked layer arrangement.[23,24] However, mimicking all of these advantageous biological structures for use in bioinspired engineering materials remains a complex design and fabrication challenge.

Here, we propose the use of irregularity to generate bioinspired interlocking materials, and we present a class of two-phase composites composed of tessellations of stiff reinforcing particles connected by a soft matrix. Going one step beyond the biological materials, we show that our materials offer control

Please cite this article in press as: Fox et al., Controllable interlocking from irregularity in two-phase composites, Matter (2025), https://doi.org/10.1016/j.matt.2025.102201

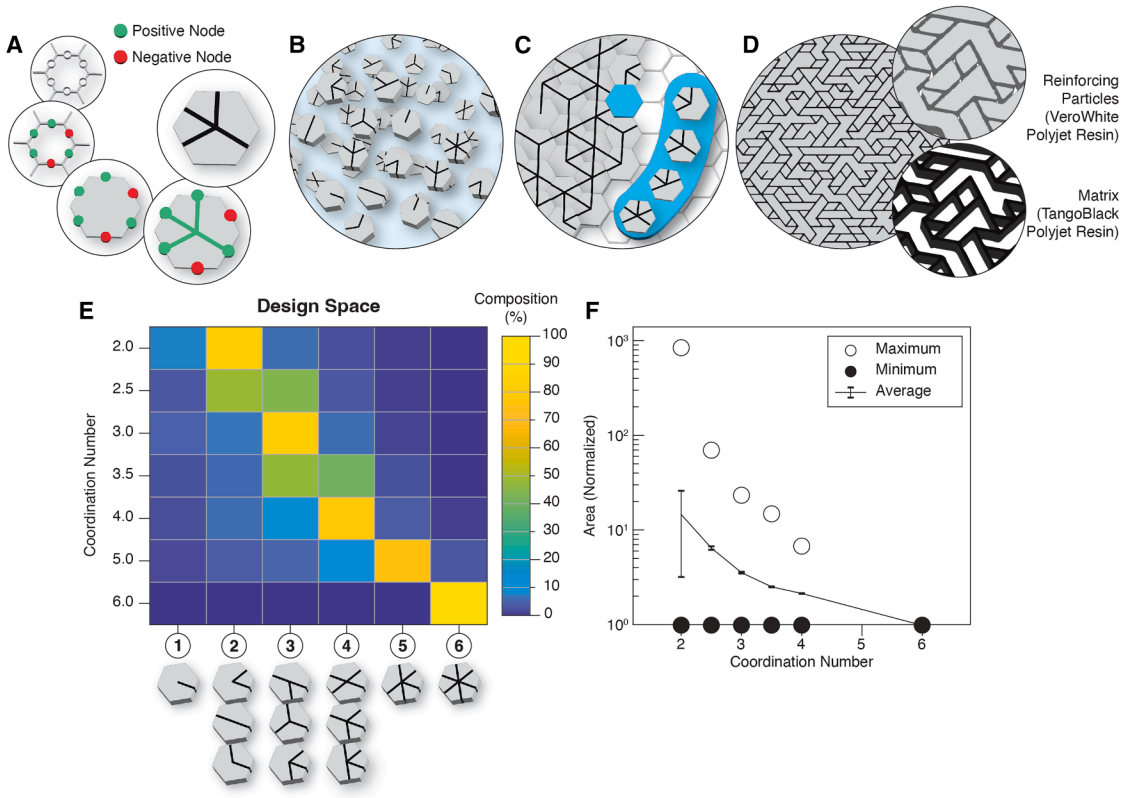

Figure 1. Sample generation and characterization of design space

(A) Node identification with positive (green) and negative (red) nodes.

(B) Assorted hexagonal tiles.

(C) Hexagonal tile connectivity.

(D) Composite material generation with reinforcing particles and matrix.

(E) Hexa-VGA sample compositions as a function of coordination number.

(F) Triangle-normalized particle size distributions as a function of coordination number.

over the degree of interlocking, defined as the kinematic constraints provided by neighboring particles,[25] through control of particle size, geometry, and arrangement. We generate the materials using a virtual growth algorithm (VGA), which mimics the growth of stochastic structures observed in nature by assembling simple building blocks into a network according to connectivity rules.[26–30] To further increase the design space, we present a VGA on a hexagonal grid (hexa-VGA), offering up to 6-sided connectivity. The hexa-VGA begins with a set of nodes on the hexagonal grid and randomly assigns connections from each node until the entire grid is filled, forming a network. We define the average number of connections per node as the coordination number,[31,32] which we use as an input parameter for the hexa-VGA. The generated hexa-VGA network then forms the matrix phase of our composite materials, while the reinforcing particles are formed by the areas enclosed by the matrix.

As a function of coordination and the resulting particle size, geometry, and arrangement, particles interlock to varying degrees in response to the kinematic constraints provided by neighboring particles. This mechanical performance is reminiscent of not only interlocking biological materials but also interlocking engineering materials, which have been previously shown to provide tunable bending stiffness,[33–36] enhanced load-bearing capacity,[35,37–39] and improved toughness.[36,40–44] However, all of the previous studies on interlocking are limited by the periodic nature of the interlocking elements in both the biological materials and the engineering materials. In contrast, our irregular elements (particles) offer a wider design space, with control over the degree of interlocking in response to loading, as a function of the coordination number.

RESULTS AND DISCUSSION

Sample design

To design and generate our samples, we use a hexa-VGA, which stochastically grows a network from a set of nodes on a hexagonal grid. The hexa-VGA is defined by a coordination number, which is the average number of connections per node (Figure 1A). We can therefore define a set of 63 geometrically or rotationally unique hexagonal tiles, which form from the network on the grid (Figures 1B and 1C). To make our polymer composite materials, we additively manufacture the generated network as the soft matrix phase, while the

Please cite this article in press as: Fox et al., Controllable interlocking from irregularity in two-phase composites, Matter (2025), https://doi.org/10.1016/j.matt.2025.102201

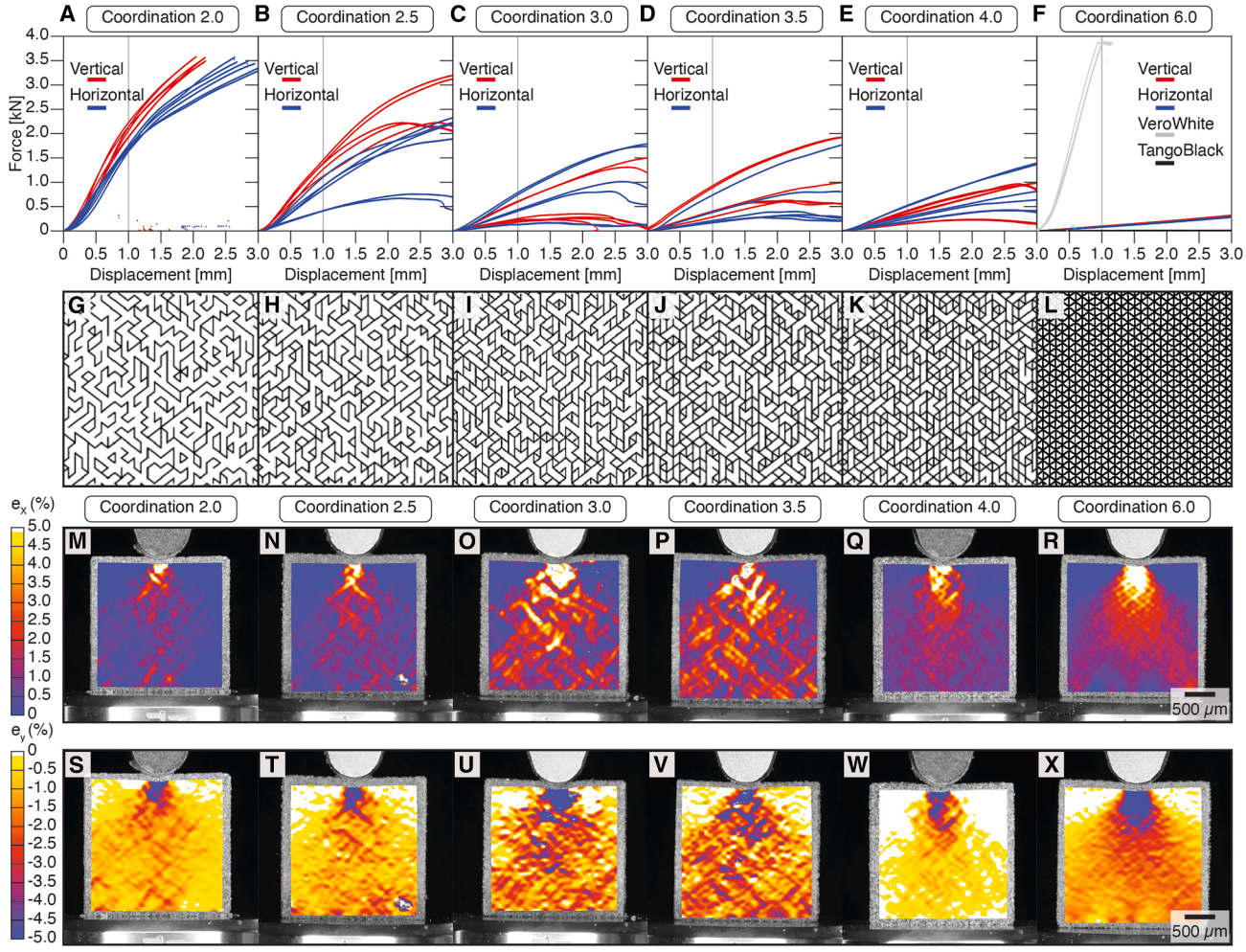

Figure 2. Cylindrical contact loading characterization

(A–F) Force-displacement plots for coordinations 2X, 2.5X, 3X, 3.5X, 4X, and 6X, respectively. Red refers to vertical matrix orientation, blue refers to horizontal matrix orientation, and gray line highlights 1 mm displacement.

(G–L) Selected samples with vertical orientation.

(M–R) 2D DIC maps of ε_x strain for corresponding selected samples.

(S–X) 2D DIC maps of ε_y strain for corresponding selected samples.

areas enclosed by the network form the stiff reinforcing phase (Figure 1D). Further details on the material properties may be found in the supplemental information (Figure S1), and details on the generation and fabrication methods may be found in the methods section.

To span the available design space, we generate samples with coordinations of 2X, 2.5X, 3X, 3.5X, 4X, 5X, and 6X, which are composed of primarily either 100% of the coordination tile type (for integer coordinations) or 50% of the tile type above and 50% of the tile type below (for non-integer coordinations) (Figure 1E). The particle size is inversely related to the coordination number, with coordination 2X below the percolation threshold for equilateral triangular networks,[45] resulting in the largest particles (Figure 1F). The smallest particle size possible is that of a triangle formed by adjacent lines (Figure 1C).

Mechanical characterization: Cylindrical contact loading

Samples are loaded in compression with a cylindrical contact to understand how the structure responds to localized load at displacements up to 3 mm (Figures 2A–2F). We test three different samples for each coordination (2X, 2.5X, 3X, 3.5X, and 4X) and observe that at the lowest coordination, the material behaves similarly to a bulk material, as it falls below the percolation threshold for an equilateral triangular network[45] and is primarily composed of a few large particles (Figure 2A). As the coordination number increases, stiffness and strength decrease as a result of both volume fraction, which decreases with increasing coordination number, and structure, since intermediate coordinations display similar stiffness and strengths (Figures 2B–2F).

To decouple the effect of volume fraction, we test 6X samples with the same volume fraction of reinforcing particles as 2X,

Please cite this article in press as: Fox et al., Controllable interlocking from irregularity in two-phase composites, Matter (2025), https://doi.org/10.1016/j.matt.2025.102201

2.5X, 3X, 3.5X, and 4X irregular samples. These equivalent samples are composed of uniform triangular particles of varying sizes according to the volume fraction of each coordination, and we maintain the same matrix width for all samples. We observe an increase in both stiffness and strength with increasing particle phase volume fraction (Figure S2) but not as large of an increase in stiffness and strength as observed in the irregular composites (Figures 2A–2F). These periodic equivalent samples also begin to fail sooner at lower coordinations, resulting in a decrease in measured force as a result of bands of particles shearing for these periodic materials rather than their interlocking irregular counterparts.

Given the hexagonal nature of the hexa-VGA used to generate the samples, we examine the effect of orientation by testing samples at 0° (horizontal, blue) and 90° (vertical, red), such that the underlying hexagonal grid is aligned along the widest hexagon direction and the narrowest hexagon direction (Figures 2A–2F). At lower coordinations, there is significant anisotropy, with the vertical orientation displaying greater stiffness and strength (Figures 2A and 2B). This trend decreases as the coordination number increases (Figures 2C–2E) until we reach the periodic 6X case, where the vertical orientation re-emerges as being stiffer (Figures 2F and S3). This anisotropy effect is likely the result of both particle size, which decreases with coordination, offering a wider range of possible geometries and orientations while maintaining irregularity at intermediate coordinations, and the matrix alignment with respect to the direction of loading, where horizontal alignment allows for greater deformability in the lateral *x* direction when loaded from the normal *y* direction. We measure the angle of alignment of the particles to quantify this anisotropy. Using "regionprops" in MATLAB (MathWorks, USA) to obtain the angle of orientation, we show that intermediate coordinations have a more uniform distribution of particle orientations for both alignments, while more extreme coordinations (i.e., 2X and 6X) show more skewed distributions (Figure S4). These differences in structure and resulting mechanical response (Figures 2A–2F) offer a way to design materials that primarily deform and fail in a desired direction and with a particular mode, depending on the desired application. For example, it is possible to obtain stronger materials from vertically aligned lower coordinations, which deform primarily through the axial compression of larger vertically aligned particles, or weaker materials from horizontally aligned higher coordinations, which deform through the shearing of smaller diagonally aligned particles.

We then use 2D digital image correlation (DIC) to track the sample deformation up to 1 mm cylindrical contact displacement (indicated by the gray line in the force-displacement plots [Figures 2A-2F]). Across the various samples (Figures 2G–2I and S5), we observe varying amounts of strain surface area (structural engagement) as a function of coordination number, with intermediate coordinations displaying the largest region of both ε_x (Figures 2M–2R and S5) and ε_y strain (Figures 2S–2X and S5).

Mechanical characterization: Matrix response

To understand the reason for the non-linear trend in structural engagement, we first characterize the matrix response as a function of coordination number. The matrix response (i.e., regions of non-zero strain) gives us an indication of how the particles are interacting and how many particles are engaging to accommodate the loading. The strain surface maps can be masked to obtain the strain maps of the soft matrix exclusively (Figures 3A–3C). After normalizing for the volume fraction of the matrix in each sample, we observe that matrix engagement (defined as non-zero matrix strain across the sample surface area) follows the same trend as the overall structure engagement and varies with coordination number. The lowest values occur at 6X, followed by 2X, and the greatest values occur around 3X to 3.5X, once we reach a cylindrical contact displacement greater than 0.33 mm, for both ε_x and ε_y strain (Figures 3D and 3E). This peak of matrix engagement is likely the result of particle geometries and arrangement, whose irregularity leads to a series of kinematic constraints as particles engage with neighboring particles, distributing strain over a large amount of the sample. We also compare these irregular composites with their periodic counterparts to understand the role of particle interlocking. In response to loading, the 6X equivalent volume fraction samples display exclusively collective sliding behavior, resulting in the formation of shear bands, similar to that of the original 6X samples (Figure S6). We then measure the amount of matrix engagement as a function of volume fraction to quantify the extent of the interlocking mechanism and decouple the effect of interlocking from the intrinsic material properties. Unlike the irregular samples, the periodic equivalent samples do not display a peak in matrix engagement at intermediate coordinations (Figure S7). This discrepancy in trends between the periodic and irregular samples can therefore be attributed to the activation of the interlocking mechanism, which is in competition with the collective sliding mechanism in the irregular samples. It is also important to note that the total percentage of matrix engagement in the periodic samples is higher than that in the irregular samples, especially at lower coordinations, but the number of particles is also greater in the periodic samples. This means that although the total amount of matrix engaged is higher, the number of particles interacting per unit of matrix engagement is actually lower.

To further quantify how the matrix distributes strain across the structure, we also measure the average strain across the sample depth. At 1 mm cylindrical contact displacement, we first convert the strain maps to grayscale values in MATLAB (MathWorks) and then collapse the strain maps to a vertical line, where darker values indicate greater amounts of strain (Figures 3F–3K). We observe that intermediate coordinations also display the greatest depth of matrix engagement (Figure 3L), with maxima around 3X and 3.5X (Figure 3M). This again indicates that these intermediate coordinations engage the largest amount of the composite structure in response to the cylindrical contact loading.

Mechanical characterization: Particle response

We then examine the particle response to further understand the relationship between coordination number and

Please cite this article in press as: Fox et al., Controllable interlocking from irregularity in two-phase composites, Matter (2025), https://doi.org/10.1016/j.matt.2025.102201

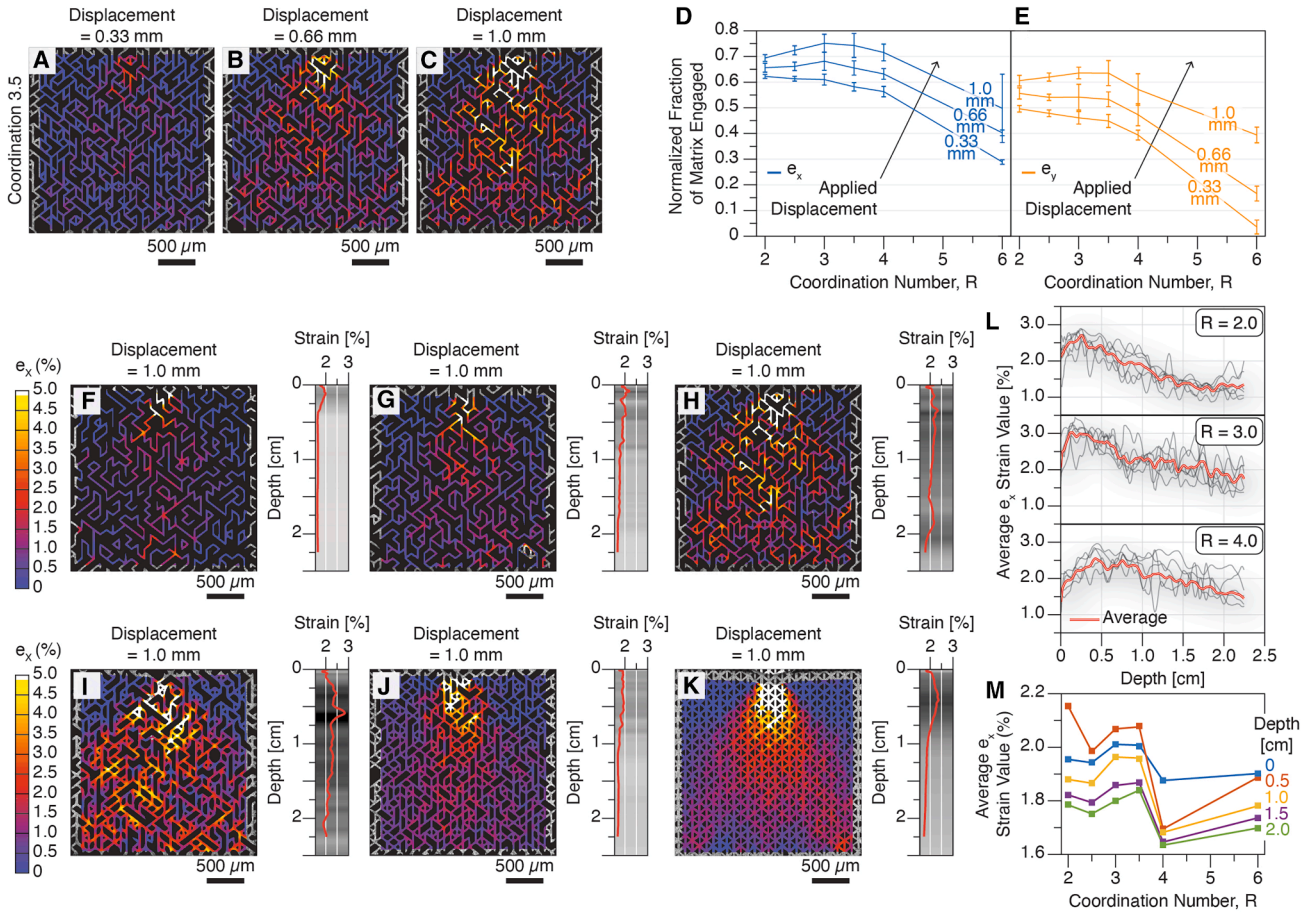

Figure 3. Matrix response characterization

(A–C) Example 3.5X matrix ε_x strain with increasing cylindrical contact displacement.

(D) Volume-normalized fraction of matrix engaged as a function of coordination number and cylindrical contact displacement for ε_x strain.

(E) Volume-normalized fraction of matrix engaged as a function of coordination number and cylindrical contact displacement for ε_y strain.

(F–K) Example 2X, 2.5X, 3X, 3.5X, 4X, and 6X matrix ε_x strains at 1 mm cylindrical contact displacement with corresponding horizontally averaged ε_x strain values (grayscale bars with line plot average).

(L) Average ε_x strain value as a function of depth for all 2X, 3X, and 4X coordinations at 1 mm cylindrical contact displacement.

(M) Average ε_x strain value as a function of coordination number for all 2X, 3X, and 4X coordinations at various sample depths.

how the structure accommodates the applied loading. In this study, we focused on the low-strain regime, and therefore, it is important to note that the tough matrix-particle interface does not fracture during loading[46] and particles remain adhered to their surrounding matrix phase throughout our analysis.

The 2X samples are primarily composed of a few large particles, given that they are below the percolation threshold, and behave similarly to a bulk material. As the coordination increases and crosses the percolation threshold, particle number increases and particle size decreases, although lower coordinations (3X) still feature highly polydisperse particles with irregular geometries, which are often concave (Figure 4A). Under cylindrical contact loading, these low-coordination samples deform as individual particles uniquely translate, rotate, and deform to accommodate the non-uniform kinematic constraints provided by neighboring particles. We define the degree to which particles are kinematically constrained by neighboring particles as interlocking,[25,37] and the lower coordinations display the greatest amount of interlocking (Figures 4A; Video S1). To quantify the interlocking behavior, individual particle path vectors can be tracked using FIJI TrackMate,[47] and we can then use these vectors to observe how the particles move relative to one another (Figure 4B). Greater interlocking results in a particle vector that is more dissimilar to neighboring particle vectors, resulting in a wide distribution of vector angles in a local region (Figure 4C). As the coordination increases further to 4X, particle size continues to decrease, and particles become more uniform in both shape and size (Figure 4D). In addition to particle-to-particle interlocking, this uniformity results in the activation of mechanisms of collective particle sliding due to the reduced

Please cite this article in press as: Fox et al., Controllable interlocking from irregularity in two-phase composites, Matter (2025), https://doi.org/10.1016/j.matt.2025.102201

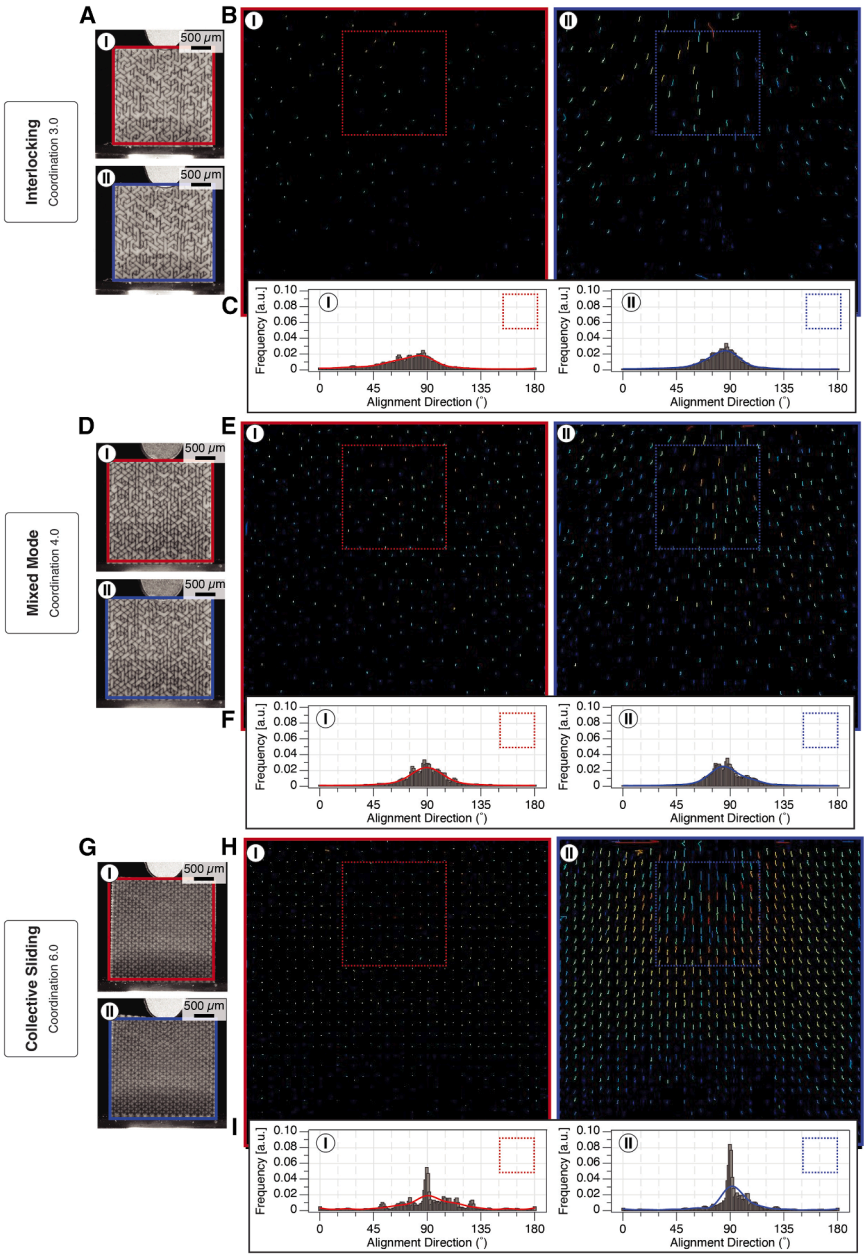

Figure 4. Particle response characterization

(A) Example 3X particle image at 0.5 (I) and 1 (II) mm cylindrical contact displacement.
(B) Corresponding particle vector map at 0.5 (I) and 1 (II) mm displacement.
(C) Histogram of vector map line angle frequencies at 0.5 (I) and 1 (II) mm displacement.
(D) Example 4X particle image at 0.5 (I) and 1 (II) mm displacement.
(E) Corresponding particle vector map at 0.5 (I) and 1 (II) mm displacement.
(F) Histogram of vector map line angle frequencies at 0.5 (I) and 1 (II) mm displacement.
(G) Example 6X particle image at 0.5 (I) and 1 (II) mm displacement.
(H) Corresponding particle vector map at 0.5 (I) and 1 (II) mm displacement.
(I) Histogram of vector map line angle frequencies at 0.5 (I) and 1 (II) mm displacement.

neighboring particle kinematic constraints in local regions (Video S2). This mixed-mode behavior is reminiscent of nacre, although the interlocking and collective sliding of nacre's tablets are sequential deformation responses resulting from monodisperse tablets[1,9,20,48] rather than a simultaneous tradeoff resulting from polydispersity and irregularity. The mixed-mode behavior results in a narrower distribution of particle vector angles, as the collectively sliding particles have more similar angles in a local region (Figures 4E and 4F). At 6X coordination, all particles collectively slide, as all particles are convex and periodically arranged, with uniform shape and size (Figures 4G and 4H; Video S3), and the distribution of particle vector angles becomes much narrower in a local region (Figure 4I).

Mechanical characterization: Statistical analysis

To quantify the transition from interlocking to collective sliding behavior in our materials, we examine the statistics behind the particle and matrix arrangement. To reduce interlocking and achieve collective sliding behavior, the matrix must be arranged in continuous straight lines to form planes along which particles can slide. Given an initial matrix orientation on a hexagonal tile, we can therefore determine which subsequent tiles allow the straight line of matrix to continue (Figure 5A) and which divert it (Figure 5B). With rotational symmetry, regardless of the initial matrix orientation, the tile distributions for continuing or diverting remain the same, resulting in a continuous or discontinuous line of matrix (Figure 5C). Given the input parameter of the coordination number, which tells us which tile types we have available, we can then calculate the probability of the matrix continuing to determine the average length of matrix lines. We use Bayes theorem,

$$P(R \cap \textit{tiling plane}) = \left[\sum_{1}^{i} P(\textit{tiling plane} | \textit{tile type}_i) * P(\textit{tile type}_i) \right]^{j}, \quad \text{(Equation 1)}$$

where i is the number of tile types and j is the number of tiles. By placing a threshold at a percentage of less than 1%

Please cite this article in press as: Fox et al., Controllable interlocking from irregularity in two-phase composites, Matter (2025), https://doi.org/10.1016/j.matt.2025.102201

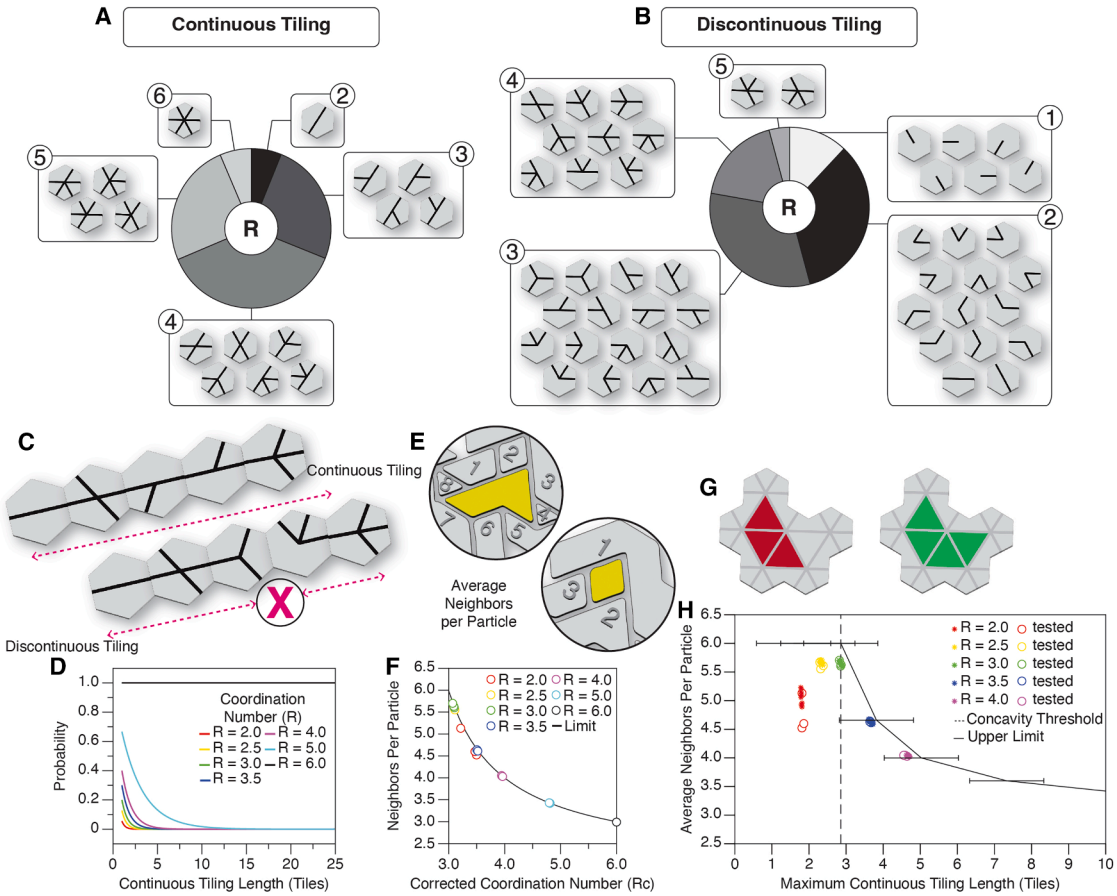

Figure 5. Statistical characterization of matrix and particles

(A) Continuous tiles for 60° example matrix plane according to coordination number.

(B) Discontinuous tiles for 60° example matrix plane according to coordination number.

(C) Example of continuous and discontinuous tiling planes.

(D) Probability of continuous tiling as a function of number of tiles for various coordination numbers.

(E) Examples of counts of neighboring particles per particle.

(F) Neighboring particles per particle as a function of corrected coordination number; solid black line denotes upper limit.

(G) Example of convex (red) particle and concave (green) and geometries.

(H) Average neighboring particles per particle as a function of maximum continuous tiling; dashed black line denotes concavity threshold, and solid black line denotes upper limit.

likelihood, we can plot the expected length of straight lines of matrix for each coordination type, and we can see that the probability increases non-linearly with coordination number (Figure 5D). Low coordinations have statistically shorter lines of continuously aligned matrix, resulting in complex geometries that interlock, while higher coordinations have statistically longer lines, with 6X showing only continuous lines, resulting in collective sliding behavior (Figure 5D).

To further understand what gives rise to interlocking behavior and how particles engage with neighboring particles, we also quantify the average number of neighboring particles per particle. Using the Euler characteristic,[49] we determine the number of particles and the number of edges (which correspond to neighbors). The Euler characteristic is defined for a 2D graph as

$$V - E + F = 1, \qquad \text{(Equation 2)}$$

where V is the number of tiles greater than 2X; E is the number of edges, defined as

$$E = \frac{R_c V}{2}, \qquad \text{(Equation 3)}$$

where R_c is the corrected coordination number, found by removing any 2X tiles, which only contribute to the length of the edges but not to the number of edges; and F is the number of particles. F can therefore be rewritten as

$$F = 1 - V\left(1 - \frac{R_c}{2}\right). \qquad \text{(Equation 4)}$$

Please cite this article in press as: Fox et al., Controllable interlocking from irregularity in two-phase composites, Matter (2025), https://doi.org/10.1016/j.matt.2025.102201

We then determine the average number of neighboring particles per particle, N (Figure 5E):

$$N = \frac{E}{F}. \quad \text{(Equation 5)}$$

From the Euler characteristic (Equation 2), the maximum average number of neighbors per particle cannot exceed six, and as the corrected coordination number increases above 3X, the maximum number of neighbors per particle decreases until we reach a limit of three neighbors at 6X (Figure 5F). This follows the trend we observed where the maximum amount of structural engagement occurs at intermediate coordinations. At these coordinations, we have both interlocking particles engaging with a nearly maximum number of neighbors, as well as collectively sliding particles, which easily move in large groups. At these intermediate coordinations, the average particle size also maintains a concave shape, which allows for more kinematic constraints (greater interlocking), formed by more than three triangles (Figure 5G). These kinematic constraints then allow the particles to easily distribute the loading to their neighboring particles across the structure.

To find the upper bounds of the design space, we plot together the maximum continuous tilings and the corresponding neighbors per particle, and we include our tested samples as well as additional samples that were only statistically analyzed (Figure 5H). To achieve the greatest degree of interlocking, lower coordinations are desirable, while the lowest degree of interlocking is achieved at 6X, when all particles collectively slide along continuous matrix lines. However, as previously discussed, the greatest amount of structural engagement occurs at intermediate coordinations, when there is a trade-off between the simultaneous activation of the interlocking and collective sliding mechanisms. It should be noted that the upper limit defined here is for the homogeneous case where samples are formed by nearly 100% of their coordination number tile type for integer coordinations or 50% above and 50% below for non-integer coordinations (Figure 1E). It is therefore possible to increase the continuous tiling length by forming the same coordination number with other tile compositions that have greater numbers of high coordination tiles, although these may not be feasible to generate using the hexa-VGA.

Conclusions

We present a class of two-phase composites composed of tessellations of stiff particles connected by a soft matrix. Drawing inspiration from the excellent mechanical performance of interlocking structures observed in many natural materials, our composites feature particle interlocking in response to loading. Going one step beyond the biological materials, we control the degree of interlocking using irregularity of particle size, geometry, and arrangement. We generate the composites through a hexa-VGA, which stochastically connects a network of nodes on a hexagonal grid according to coordination number. We then use the generated hexa-VGA network as the matrix phase, while the reinforcing particles are formed by the areas enclosed by the matrix. Lower coordinations feature highly polydisperse particles, which interlock as a result of their irregular geometries and non-periodic tessellations. Higher coordinations feature more monodisperse particles, which collectively slide as a result of their more uniform geometries and tessellations. Finally, we show and statistically quantify how to control the trade-off between these interlocking and sliding mechanisms, with the activation of a particular mechanism and the amount of structural engagement controlled by coordination number alone. These findings offer an exciting new research direction, especially for 3D extensions of these 2D findings on controllable interlocking, for new materials with spatially tailorable stiffness, strength, ductility, and toughness.

METHODS

Sample generation and fabrication

The hexa-VGA code used to generate the samples is written in Python and may be found at the following link: https://github.com/basbaskoko/hexaVGA.

The hexa-VGA generates (irregular) networks by beginning with an equilateral triangular network placed on a hexagonal grid. Lists of unique lines in the network are first defined by their endpoints and then initiated with a status of "neither." An arbitrary endpoint (a node) is randomly selected, from which X (out of 6) lines are assigned the status "positive," while the rest are given the status "negative." This number X is defined as the coordination number, and we define it on a set of tiles formed by the hexagonal grid. Once a line has been assigned a status, that status cannot change. After all lines beginning at an endpoint have been assigned a status, that endpoint is removed from the set of "free" endpoints. If any of the neighboring 6 endpoints are free endpoints, one of them is chosen to have its lines assigned a status. If none of the neighboring endpoints are free endpoints, a random free endpoint is selected, and this process continues until no free endpoints remain and all lines have been assigned a status, resulting in a network of interconnected nodes.

To fabricate our composite samples from the hexa-VGA output network, we first use the network information to create an STL file for the soft matrix, which is made from TangoBlack PolyJet resin, and then take its negative to form the stiff reinforcing particles, which is made from VeroWhite PolyJet resin. We conducted simple tension tests to obtain the constitutive stress-strain properties of both resins (Figure S1), and the mechanical properties of the two phases fall within those reported in the literature.[50–52] Due to printer resolution constraints, we choose a matrix width of 100 μm and a minimum particle width of 1 mm.

It is also important to consider the effect of the sample geometry, given that the fabricated samples have a square shape, while the tiles that tessellate it are hexagonal and therefore cannot perfectly fill the square space, resulting in a smaller average edge particle size. However, the number of total tiles is significantly higher than the number of edge tiles, which represent just 18% of the total tile population.

Cylindrical contact compression testing

We use an Instron E3000 with a 5 kN load cell (Instron, USA) to apply compression loading. Samples of 2.5 × 2.5 × 1 cm are loaded with a cylindrical contact of 1 cm diameter. Testing is

conducted for displacements up to 3 mm, which is just prior to fracture. Three different samples are tested for each coordination to ensure consistency across samples.

DIC

To conduct 2D DIC on the samples, we apply a layer of matte white paint and then matte black speckles with a diameter of 0.1–0.3 mm to the front face of the samples. During loading, we use a Nikon D750 DSLR camera (Nikon, Japan) with a 120 mm lens to take images at a rate of 1 frame per second. We use VIC 2D (Correlated Solutions, USA) to conduct the DIC analysis, using a step size of 2 and a subset size of 29, and obtain the Lagrangian strain fields in the x direction and y direction.

RESOURCE AVAILABILITY

Lead contact

Requests for further information and resources should be directed to and will be fulfilled by the lead contact, Chiara Daraio (daraio@caltech.edu).

Materials availability

This study did not generate new unique reagents.

Data and code availability

- All data reported in this paper will be shared by the lead contact upon request.
- The hexa-VGA code used to generate the samples may be found at the following link: https://github.com/basbaskoko/hexaVGA.

ACKNOWLEDGMENTS

The authors acknowledge MURI ARO W911NF-22-2-0109 for financial support. The authors acknowledge P. Arakelian for experimental assistance.

AUTHOR CONTRIBUTIONS

Conceptualization, C.F. and T.M.; methodology, C.F. and T.M.; software, C.F., K.B., and T.M.; formal analysis, C.F. and T.M.; writing – original draft, C.F., K.B., and T.M.; writing – review & editing, C.F., K.B., T.M., and C.D.; visualization, C.F. and T.M.; supervision, T.M. and C.D.; funding acquisition, C.D.

DECLARATION OF INTERESTS

The authors declare no competing interests.

SUPPLEMENTAL INFORMATION

Supplemental information can be found online at https://doi.org/10.1016/j.matt.2025.102201.

Received: February 25, 2025
Revised: April 17, 2025
Accepted: May 16, 2025

REFERENCES

1. Barthelat, F., Tang, H., Zavattieri, P., Li, C., and Espinosa, H. (2007). On the mechanics of mother-of-pearl: A key feature in the material hierarchical structure. J. Mech. Phys. Solids *55*, 306–337.
2. Oftadeh, R., Perez-Viloria, M., Villa-Camacho, J.C., Vaziri, A., and Nazarian, A. (2015). Biomechanics and Mechanobiology of Trabecular Bone: A Review. J. Biomech. Eng. *137*, 0108021–01080215.
3. Hart, N.H., Nimphius, S., Rantalainen, T., Ireland, A., Siafarikas, A., and Newton, R.U. (2017). Mechanical basis of bone strength: influence of bone material, bone structure and muscle action. J. Musculoskelet. Neuronal Interact. *17*, 114–139.
4. Magrini, T., Libanori, R., Kan, A., and Studart, A.R. (2021). Complex Materials: The Tough Life of Bone. Rev. Bras. Ensino Fís. *43*, 1–17.
5. Launey, M.E., Buehler, M.J., and Ritchie, R.O. (2010). On the mechanistic origins of toughness in bone. Annu. Rev. Mater. Res. *40*, 25–53.
6. Lin, E., Li, Y., Weaver, J.C., Ortiz, C., and Boyce, M.C. (2014). Tunability and enhancement of mechanical behavior with additively manufactured bio-inspired hierarchical suture interfaces. J. Mater. Res. *29*, 1867–1875.
7. Ritchie, R.O. (2011). The conflicts between strength and toughness. Nat. Mater. *10*, 817–822.
8. Mirkhalaf, M., Dastjerdi, A.K., and Barthelat, F. (2014). Overcoming the brittleness of glass through bio-inspiration and micro-architecture. Nat. Commun. *5*, 3166–3169.
9. Barthelat, F. (2015). Architectured materials in engineering and biology: fabrication, structure, mechanics and performance. Int. Mater. Rev. *60*, 413–430.
10. Barthelat, F., Yin, Z., and Buehler, M.J. (2016). Structure and mechanics of interfaces in biological materials. Nat. Rev. Mater., 16007–16016.
11. Achrai, B., Bar-On, B., and Wagner, H.D. (2014). Bending mechanics of the red-eared slider turtle carapace. J. Mech. Behav. Biomed. Mater. *30*, 223–233.
12. Barthelat, F., and Rabiei, R. (2011). Toughness amplification in natural composites. J. Mech. Phys. Solids *59*, 829–840.
13. Espinosa, H.D., Rim, J.E., Barthelat, F., and Buehler, M.J. (2009). Merger of structure and material in nacre and bone – Perspectives on de novo biomimetic materials. Prog. Mater. Sci. *54*, 1059–1100.
14. Chen, I.H., Yang, W., and Meyers, M.A. (2015). Leatherback sea turtle shell: A tough and flexible biological design. Acta Biomater. *28*, 2–12.
15. Rivera, J., Hosseini, M.S., Restrepo, D., Murata, S., Vasile, D., Parkinson, D.Y., Barnard, H.S., Arakaki, A., Zavattieri, P., and Kisailus, D. (2020). Toughening mechanisms of the elytra of the diabolical ironclad beetle. Nature *586*, 543–548.
16. Jentzsch, M., Becker, S., Thielen, M., and Speck, T. (2022). Functional Anatomy, Impact Behavior and Energy Dissipation of the Peel of Citrus × limon: A Comparison of Citrus × limon and Citrus maxima. Plants *11*, 991.
17. Thielen, M., Schmitt, C.N.Z., Eckert, S., Speck, T., and Seidel, R. (2013). Structure-function relationship of the foam-like pomelo peel (Citrus maxima)-an inspiration for the development of biomimetic damping materials with high energy dissipation. Bioinspir. Biomim. *8*, 025001.
18. Lee, N., Horstemeyer, M.F., Rhee, H., Nabors, B., Liao, J., and Williams, L.N. (2014). Hierarchical multiscale structure–property relationships of the red-bellied woodpecker (Melanerpes carolinus) beak. J. R. Soc. Interface *11*, 20140274.
19. Perricone, V., Sarmiento, E., Nguyen, A., Hughes, N.C., and Kisailus, D. (2024). The convergent design evolution of multiscale biomineralized structures in extinct and extant organisms. Commun. Mater. *5*, 227–318.
20. Barthelat, F. (2010). Nacre from mollusk shells: a model for high-performance structural materials. Bioinspir. Biomim. *5*, 035001.
21. Espinosa, H.D., Juster, A.L., Latourte, F.J., Loh, O.Y., Gregoire, D., and Zavattieri, P.D. (2011). Tablet-level origin of toughening in abalone shells and translation to synthetic composite materials. Nat. Commun. *2*, 173–179.
22. Miura, T., Perlyn, C.A., Kinboshi, M., Ogihara, N., Kobayashi-Miura, M., Morriss-Kay, G.M., and Shiota, K. (2009). Mechanism of skull suture maintenance and interdigitation. J. Anat. *215*, 642–655.
23. Currey, J.D., Nash, A., and Bonfield, W. (1982). Calcified cuticle in the stomatopod smashing limb. J. Mater. Sci. *17*, 1939–1944.
24. Amorim, L., Santos, A., Nunes, J.P., and Viana, J.C. (2021). Bioinspired approaches for toughening of fibre reinforced polymer composites. Mater. Des. *199*, 109336.

25. Dyskin, A.V., Estrin, Y., and Pasternak, E. (2019). Topological interlocking materials. Springer Mater. Sci. *282*, 23–49.

26. Liu, K., Sun, R., and Daraio, C. (2022). Growth rules for irregular architected materials with programmable properties. Science *377*, 975–981.

27. Wang, R., Bian, Y., and Liu, K. (2025). Nonlinear mechanical properties of irregular architected materials. J. Appl. Mech. *92*, 1–20.

28. Jia, Y., Liu, K., and Zhang, X.S. (2024). Topology optimization of irregular multiscale structures with tunable responses using a virtual growth rule. Comput. Methods Appl. Mech. Eng. *425*, 116864.

29. Jia, Y., Liu, K., and Zhang, X.S. (2024). Unstructured growth of irregular architectures for optimized metastructures. J. Mech. Phys. Solids *192*, 105787.

30. Fox, C., Chen, K., Antonini, M., Magrini, T., and Daraio, C. (2024). Extracting Geometry and Topology of Orange Pericarps for the Design of Bioinspired Energy Absorbing Materials. Adv. Mater. *36*, 2405567.

31. Thorpe, M.F. (1983). Continuous deformations in random networks. J. Non-Cryst. Solids *57*, 355–370.

32. Thorpe, M., and Duxbury, P. (2002). Rigidity theory and applications (Springer). https://doi.org/10.1007/B115749.

33. Lu, T., Zhou, Z., Bordeenithikasem, P., Chung, N., Franco, D.F., Andrade, J.E., and Daraio, C. (2024). Role of friction and geometry in tuning the bending stiffness of topologically interlocking materials. Extreme Mech. Lett. *71*, 102212.

34. Khandelwal, S., Siegmund, T., Cipra, R.J., and Bolton, J.S. (2015). Adaptive mechanical properties of topologically interlocking material systems. Smart Mater. Struct. *24*, 045037.

35. Siegmund, T., Barthelat, F., Cipra, R., Habtour, E., and Riddick, J. (2016). Manufacture and Mechanics of Topologically Interlocked Material Assemblies. Appl. Mech. Rev. *68*, 040803.

36. Estrin, Y., Beygelzimer, Y., Kulagin, R., Gumbsch, P., Fratzl, P., Zhu, Y., and Hahn, H. (2021). Architecturing materials at mesoscale: some current trends. Mater. Res. Lett. *9*, 399–421.

37. Estrin, Y., Krishnamurthy, V.R., and Akleman, E. (2021). Design of architectured materials based on topological and geometrical interlocking. J. Mater. Res. Technol. *15*, 1165–1178.

38. Djumas, L., Simon, G.P., Estrin, Y., and Molotnikov, A. (2017). Deformation mechanics of non-planar topologically interlocked assemblies with structural hierarchy and varying geometry. Sci. Rep., 11844–11911.

39. Feldfogel, S., Karapiperis, K., Andrade, J., and Kammer, D.S. (2023). Scaling, saturation, and upper bounds in the failure of topologically interlocked structures. Int. J. Solids Struct. *269*, 112228.

40. Dyskin, A.V., Estrin, Y., Kanel-Belov, A.J., and Pasternak, E. (2001). Toughening by Fragmentation How Topology Helps. Advanced Engineering Materials *3*, 885–888.

41. Dyskin, A.V., Estrin, Y., Pasternak, E., Khor, H.C., and Kanel-Belov, A.J. (2003). Fracture Resistant Structures Based on Topological Interlocking with Non-planar Contacts. Adv. Eng. Mater. *5*, 116–119.

42. Mirkhalaf, M., Zhou, T., and Barthelat, F. (2018). Simultaneous improvements of strength and toughness in topologically interlocked ceramics. Proc. Natl. Acad. Sci. USA *115*, 9128–9133.

43. Rosewitz, J.A., Choshali, H.A., and Rahbar, N. (2019). Bioinspired design of architected cement-polymer composites. Cem. Concr. Compos. *96*, 252–265.

44. Askarinejad, S., Choshali, H.A., Flavin, C., and Rahbar, N. (2018). Effects of tablet waviness on the mechanical response of architected multilayered materials: Modeling and experiment. Compos. Struct. *195*, 118–125.

45. Sykes, M.F., Essam, J.W., and Essam, J.W. (1964). Exact Critical Percolation Probabilities for Site and Bond Problems in Two Dimensions Exact Critical Percolation Probabilities for Site and Bond Problems in Two Dimensions. J Math Phys *5*, 36.

46. Nash, R.J., and Li, Y. (2021). Experimental and numerical analysis of 3D printed suture joints under shearing load. Eng. Fract. Mech. *253*, 107912.

47. Ershov, D., Phan, M.S., Pylvänäinen, J.W., Rigaud, S.U., Le Blanc, L., Charles-Orszag, A., Conway, J.R.W., Laine, R.F., Roy, N.H., Bonazzi, D., et al. (2022). TrackMate 7: integrating state-of-the-art segmentation algorithms into tracking pipelines. Nat. Methods *19*, 829–832.

48. Wegst, U.G.K., Bai, H., Saiz, E., Tomsia, A.P., and Ritchie, R.O. (2014). Bioinspired structural materials. Nat. Mater. *14*, 23–36.

49. Euler, L. (1758). Elementa doctrinae solidorum. Novi Commentarii Academiae Scientiarum Petropolitanae. Opera Mathematica *26*, 71–93.

50. Dizon, J.R.C., Espera, A.H., Chen, Q., and Advincula, R.C. (2018). Mechanical characterization of 3D-printed polymers. Addit. Manuf. *20*, 44–67.

51. Bell, D., and Siegmund, T. (2018). 3D-printed polymers exhibit a strength size effect. Addit. Manuf. *21*, 658–665.

52. Slesarenko, V., and Rudykh, S. (2018). Towards mechanical characterization of soft digital materials for multimaterial 3D-printing. Int. J. Eng. Sci. *123*, 62–72.